scientific reports

Check for updates

OPEN

Degradation of dye through mechano-catalysis using $BaBi_4Ti_4O_{15}$ catalyst

Pushpendra Kumar[1], Norah Salem Alsaiari[2], Akshay Gaur[1], Karan[3], Rahul Vaish[1]✉, Abdelfattah Amari[4], Haitham Osman[4], Yun Hwan Joo[5], Tae Hyun Sung[5], Anuruddh Kumar[6]✉ & Wei-Chieh Liu[7]

Ferroelectric $BaBi_4Ti_4O_{15}$ was prepared using solid-state calcination at 950 °C for four hours. X-ray diffraction, Raman spectroscopy, and X-ray photoelectron spectroscopy were utilized to understand its microstructure and other structural aspects. Particle size was around < 1.5 µm. This oxide is able to demonstrate piezocatalysis and tribocatalysis as reflected in its dye degradation performance. This oxide showed piezocatalytic activity around 40% in 2 h and tribocatalytic activity around 90% in 12 h. The rate constant for the piezocatalytic reaction is 0.003 min^{-1} and for tribocatalytic reaction is 0.169 h^{-1}. The rotation speed also affected the tribocatalytic activity of the oxide. Oxide showed 25%, 90%, and 94% tribocatalytic activity at 300, 500, and 700 rpm respectively. This material has demonstrated notable performance of catalysis under different types of mechanical energy sources and under different mechanisms.

Keywords $BaBi_4Ti_4O_{15}$, Tribocatalysis, Bismuth layered ferroelectrics, Piezocatalysis, Textile effluent

Catalytic processes for organic pollutants degrade using semiconductor materials are the potential topic of investigation. The photocatalytic process is one of the largely explored topics for material chemists. A large number of materials have been reported in the last more than two decades[1–4]. TiO_2 is a commercially available photocatalyst that has been utilized for self-cleaning[5], dye degradation[6], volatile organic compounds degradation[7], H_2 generation[8], etc. Although, TiO_2 is a proven successful compound. There is still plenty of scope to utilize catalysis for environmental sustainability. Some of the associated challenges are visible light active catalysis, prolonged e^--hole recombination time, and waste energy utilization such as mechanical and thermal energies[9]. In this context, ferroelectric ceramics have demonstrated interesting multi-catalytic processes[10–15]. Owing to their non-centrosymmetric nature, these are bound to exhibit piezoelectric and pyroelectric properties.

In view of these, there are a large number of articles on piezocatalytic particularly on dye degradation and other electrochemistry aspects. Some of the notable materials are $BaTiO_3$[11,16–20], ZnO[21–25], $LiNbO_3$[26,27], $K_{0.5}Na_{0.5}NbO_3$[28], and their derivative compounds. These are also promising for the pyrocatalysis process which is a relatively unexplored topic. Another important catalysis process is tribocatalysis which is the derivative of the triboelectric effect. Triboelectric has shown scientific merits and shown outstanding performance for mechanical energy harvesting[29–32].

Triboelectric nanogenerators are reported using almost all kinds of nano-materials[33–36]. Tribocatalysis works on the triboelectric effect and it is mechano-chemical coupling through the triboelectric effect[29]. Tribocatalysis is relatively well-reported for various oxide ceramics[31,37–39]. To further study the potential improvement using tribo-catalysis, ferroelectric ceramic can play an important role. Remnant polarization can increase the recombination time of opposite charges. Some of these materials have been reported in recent years[40–42]. $BaBi_4Ti_4O_{15}$ (BBT) is a ferroelctric ceramic. The piezoelectric properties of this ceramic can be utilized for the piezocatalysis. Much research has been done to enhance its piezoelectric properties. The effect of microstructure on the piezoelectric

[1]School of Mechanical and Materials Engineering, Indian Institute of Technology Mandi, Mandi, Himachal Pradesh 175005, India. [2]Department of Chemistry, College of Science, Princess Nourah bint Abdulrahman University, P.O. Box 84428, 11671 Riyadh, Saudi Arabia. [3]Department of Metallurgical and Materials Engineering, Panjab Engineering Collage, Chandigarh 160012, India. [4]Department of Chemical Engineering, College of Engineering, King Khalid University, 61411 Abha, Saudi Arabia. [5]Department of Electrical Engineering, Hanyang University, 04763 Seoul, South Korea. [6]Center for Creative Convergence Education, Hanyang University, 04763 Seoul, South Korea. [7]Department of Electrical Engineering, Hanyang University, Seoul, South Korea. ✉email: rahul@iitmandi.ac.in; anuruddh07@hanyang.ac.kr

properties of BBT suggested that coarse microstructure ceramic shows higher piezoelectric properties than fine microstructure[43]. One researcher synthesized BBT heterojunctions with $BaTiO_3$ and observed that piezoelectric response increased by the formation heterojunction[44]. Bismuth is highly volatile at high temperatures so it vaporizes during the calcination process. This vaporized bismuth lowers the piezoelectric properties. So, one researcher added extra bismuth to compensate for vaporized bismuth. This strategy also improved the piezoelectric properties[45]. This ceramic is lead-free and does not contain toxic materials. Furthermore, the Curie temperature of this ceramic is also very high so the piezoelectric properties of this ceramic will be maintained at high temperatures generated locally during the piezocatalysis process. This ceramic possesses low processing temperature which results in low synthesis cost and the excellent piezoelectric properties of this ceramic motivated the author to investigate its piezocatalytic and tribocatalytic activity.

$BaBi_4Ti_4O_{15}$ (BBT) is one of the Aurivillius family materials and has been known for ferroelectric properties. Our previous studies have proven its potential merits for catalysis[46,47]. This study demonstrates the tribocatalytic properties of $BaBi_4Ti_4O_{15}$ (BBT) along with its comparison with piezocatalysis.

Experimental

BBT catalyst was synthesized via a solid-state reaction route. $BaCO_3$, Bi_2O_3, and TiO_2 were used as precursors and were mixed in the stoichiometric ratios. Bismuth is highly vaporizing at high temperatures so it can evaporate at calcination temperature. Hence, 8% extra Bi_2O_3 (by weight) was added to the precursor to compensate vaporized bismuth during the calcination process. The mixture of precursors was subjected to the 950 °C for 4 h for the calcination process.

The X-ray diffraction (XRD) technique was used to examine the phase of the synthesized catalyst. For this purpose, the Rigaku diffractometer was used. That used copper K alpha as an anode. The data was collected in the range of 20°–75° with 2°/min step size. The chemical structure and mode of vibrations were analyzed by Raman spectroscopy. Lab HR evolution by Horiba with a 532 nm wavelength laser was used for Raman spectroscopy. This experiment was done at room temperature. X-ray photoelectron spectroscopy (XPS) was used to determine the atomic (elemental) composition of the catalyst. For this purpose, XPS spectroscopy form thermofisher (Nexa) was utilized. The morphology of the synthesized catalyst was analyzed by scanning electron microscopy (SEM) by utilizing FE-SEM Inspect S50 equipment. This spectroscopy was equipped with energy dispersive analysis of x-rays (EDAX). That was utilized for the determination of elemental composition. Furthermore, the direct optical bandgap of the catalyst was determined by Tauc's plot technique. The adsorption of the catalyst was measured with UV–Vis spectroscopy. It was measured with SHIMADZU-2450 double beam spectroscopy and barium sulfate ($BaSO_4$) reference.

The piezocatalysis and tribocatalysis experiments were conducted on methylene blue (MB) dye aqueous solution. The concentration of this solution was 10 mg/L. 0.1 g of synthesized catalyst was mixed with 10 mL of this solution. Now, this is a heterogenous solution of catalyst and MB dye. Catalyst particles absorb MB dye molecules on their surface. So, this heterogeneous solution was put on the stirrer to achieve the equilibrium between adsorption and desorption. Notably, the stirrer was placed inside a dark box because the catalyst is also active in visual light and this light can degrade MB dye molecules. This solution was used for the piezocatalysis experiments.

The pressure (sonic) wave from ultrasonicator was also used to activate the catalyst particle in piezocatalysis experiments. The heterogeneous solution (MB dye and catalyst) stored in the glass beaker was placed inside the sonicator bath. The pressure wave travels through the water bath and glass beaker and enters the heterogeneous solution. This solution contains catalyst particles that were activated by these pressure waves. The frequency of the pressure wave was 40 kHz and the power of ultrasonicator was 150 W. The sonicator water bath was maintained at room temperature to avoid errors from heat gradients. The piezocatalysis experiments were conducted for a time period of 2 h and the concentration of the MB dye aqueous solution was recorded after every 30 min duration.

The tribocatalytic activity of the synthesized catalyst was tested on the MB dye solution as used in the piezocatalysis experiments. The concentration of the MB dye aqueous solution was 10 mg/L and 40 mL of such solution was taken with 0.4 g of catalyst. The adsorption and desorption equilibrium was achieved through a continuous stirrer of dye solution with catalyst. A glass beaker of 400 mL and polytetrafluoroethylene (PTFE) was used for generating triboelectric charges. A circular disc of PTFE with ~ 8 cm^2 surface area was glued with the magnetic bead so that it could rotate in the influence of the magnetic field generated by the magnetic stirrer. This glued PTFE disc with magnetic bead was used to perform tribocatalysis experiments. However, adsorption of MB dye aqueous solution was checked with a PTFE disc and was not significant. The tribocatalysis experiments were performed for 12 h at 500 rpm, and the concentration of the MB dye solution was checked after every one-hour duration. The effect of the stirring speed (rotational speed, rpm) on tribocatalytic activity was evaluated by performing tribocatalytic experiments at different stirring speeds.

The percentage degradation of MB dye aqueous solution was found by utilizing Eq. (1). The absorbance of the aqueous solution was determined by the UV–Vis spectroscopy. The value of the rate constant for the catalysis reaction was found by utilizing an integrated first-degree reaction Eq. (2).

$$\% \text{ degradation } = \left(\frac{\text{Ao} - A}{\text{Ao}}\right) \times 100 == \frac{\text{Co} - C}{\text{Co}} \times 100 \tag{1}$$

$$\ln\left(\frac{\text{Co}}{\text{C}}\right) = \text{kt} \tag{2}$$

here A_o denotes the initial absorbance and A denotes the absorbance after the t time period of catalysis. The same way C_o denotes the initial concentration of MB dye aqueous and C denotes the concentration after the t time period. The rate constant of the catalytic reaction is denoted by the k which has hr^{-1}/min^{-1} unit.

Results and discussion

The data recorded by X-ray diffraction (XRD) was plotted against 2-theta on X-axis and interference intensity on Y-axis which is shown in Fig. 1. The peaks of Fig. 1 were matched with the International Center for diffraction data (ICDD). The data matches with JCPDS number 35-0757. This JCPDS number is related to the bismuth-layered ferroelectrics. This indicates that the synthesized catalyst has an orthorhombic perovskite crystal structure and is related to the $A2_1am$ space group. There is no impurity that was observed in the synthesized catalyst. This indicates the successful synthesis of $BaBi_4Ti_4O_{15}$ (BBT) catalyst with 8% excess bismuth. The previous studies suggested that the BBT catalyst formation mechanism is $Bi_4Ti_3O_{12} + BaTiO_3 = BaBi_4Ti_4O_{15}$[43,48]. The excess bismuth added during synthesis was used to compensate for the vaporized bismuth during the calcination process (bismuth is highly volatile at high temperatures and gets evaporated during the calcination process) occupied in the pseudo perovskite block. The graph also indicated that the Bi^{3+} occupied pseudo perovskite blocks[49–51]. In the XRD plot, it can be observed that the highest intensity is related to the (119) plan, which is related to the $(Bi_2O_2)^{2-}$ bismuth layer with four intermediate four (m = 4) pseudo perovskite blocks[45,52,53]. Previous studies determined the lattice parameters by using least square refinement and suggested that there is a small increase in the 'a' parameter in comparison to the BBT without any excess bismuth[45]. This increase is because of Bi^{+3} ions that is occupied in the perovskite blocks.

Scanning electron microscopy was used to observe the morphology of the synthesized catalyst. Figure 2 shows the image recorded by the SEM. This image shows that the synthesized catalyst has a plate-like morphology. This morphology is due to a family of planes observed in the XRD plot. The XRD plot shows the highest intensity peak is related to the (119) plane. This plan is characterized by its minimum energy state. So, during the calcination process, the atoms start to diffuse on the plane that requires minimum energy. Due to diffusion on a specific plane, a plate-like morphology is observed.

Tauc's plot was used to calculate the direct bandgap of the synthesized catalyst. This plot was plotted with the help of absorption data (shown in Fig. 3a) taken by UV–Vis spectroscopy. The Tauc-Davis-Mott relation (Eq. 3) was used to plot Tauc's plot, which is shown in Fig. 3b.

$$(\alpha h\nu)^n = K(h\nu - E_g) \tag{3}$$

here α is the absorption coefficient, h is Plank's constant, ν is the frequency, K is the independent energy constant and, E_g is the optical bandgap in eV. The symbol n denotes the nature of the transmission which is direct in the case of synthesized catalyst. For direct transmission, the value of the n is 2.

The plotted Tauc's plot can be seen in Fig. 3b. This plot indicates that when a photon consisting of 2.36 eV of energy impinges on the catalyst surface, an electron jumps directly to the conduction band from the valance band by leaving a hole in the valance band. Previous studies reported that BBT without excess bismuth shows a direct bandgap of 3.29 eV[54]. Notably, there is a difference of 0.99 eV between BBT excess bismuth and BBT without excess bismuth. This difference is due to the compensated bismuth content in the BBT catalyst. Furthermore, an increased number of oxygen vacancies promotes overlapping and delocalization of the valance band edge. Which also narrows down the gap between the valance band and the conduction band. This analysis suggested that the excess bismuth decreased the direct bandgap of the catalyst and the new bandgap is in the visual region.

The data recorded by Raman spectroscopy was plotted against Raman shift on the X-axis and intensity on the Y-axis. Figure 4 illustrates this plot. Previous Raman studies on BBT catalyst suggested 11 individual modes[55].

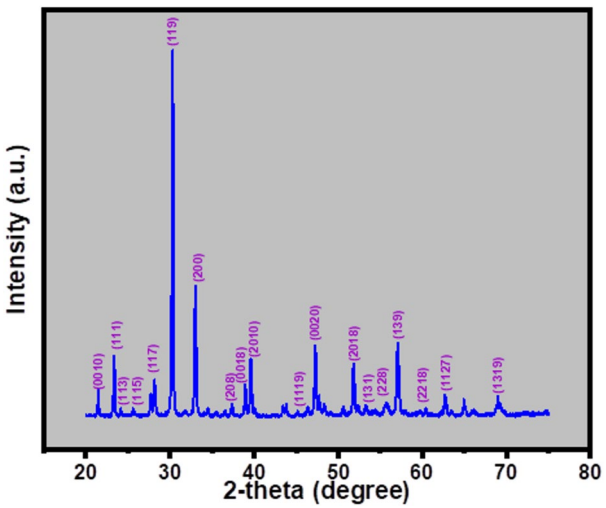

Figure 1. X-ray diffraction (XRD) plot of BBT.

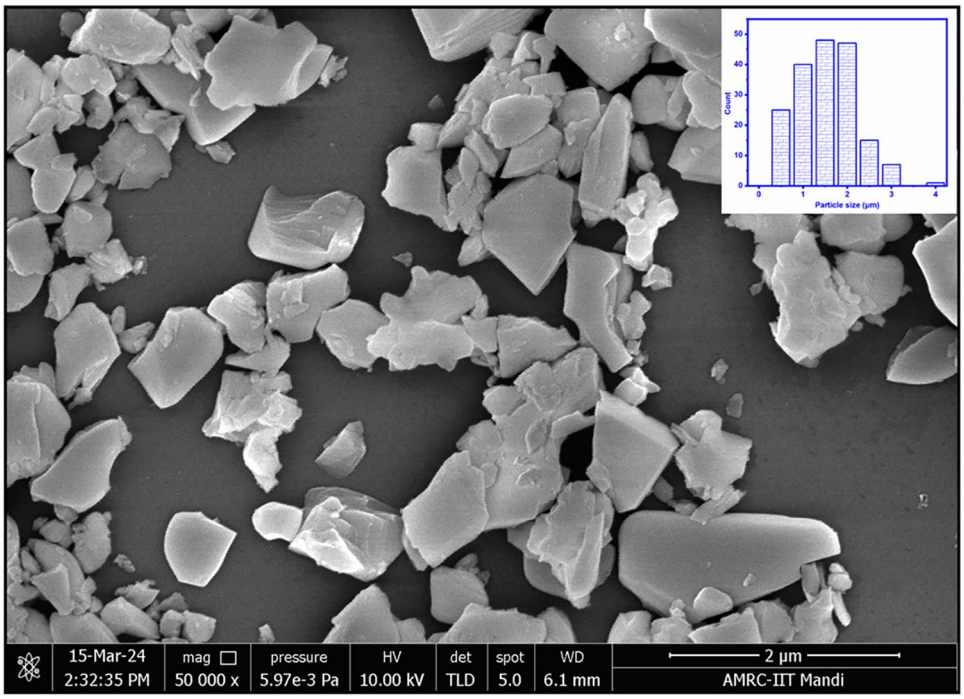

Figure 2. Scanning electron microscopy image of BBT.

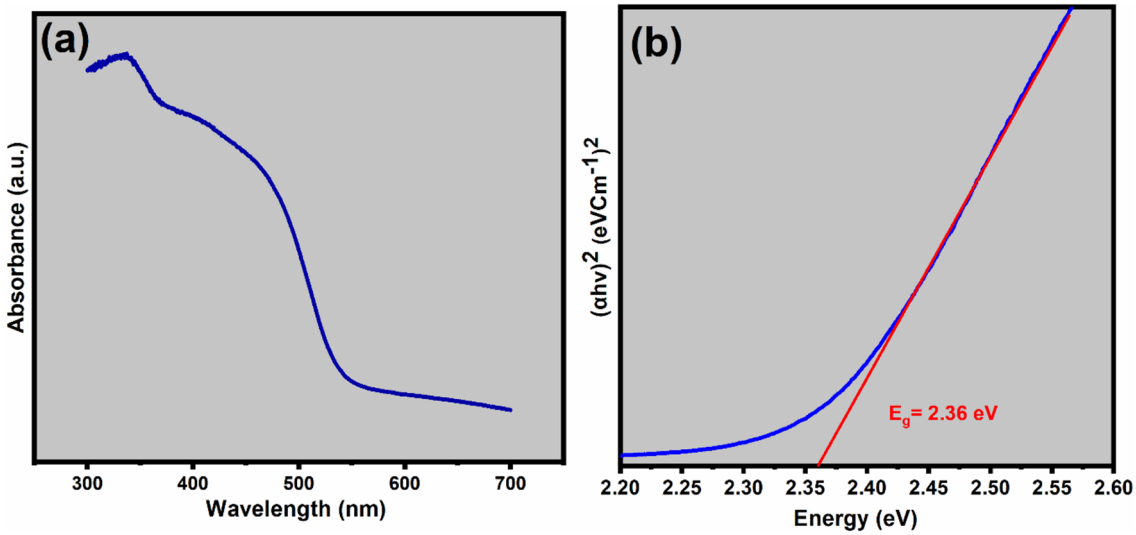

Figure 3. (**a**) Absorption spectrum, and (**b**) Tauc's plot for BBT.

Another study indicated modes for central zone phonons of $37A_1 + 35A_2 + 35B_1 + 37B_2$ for BBT in $A2_1am$ symmetry. This study suggested that only $1A_1 + 1B_1 + 1B_2$ mode is acoustic in nature, all other modes are due to BBT[56]. The addition of bismuth in the BBT results in producing distortion in the lattice of the BBT crystal structure. Furthermore, this distortion results in induced less intensity, mode of overlapping, and overdamping, broken symmetry, making many modes indistinguishable. This type of spectrum has been seen in many studies of other Aurivillius phases also[57–61]. The peaks (in Fig. 4) below 200 cm^{-1} are related to the bismuth layer and peaks above 200 cm^{-1} are related to the perovskite block. However, the peak at 887.96 cm^{-1} is related to the symmetrical stretching of TiO_6 octahedral[62]. The plot shows a peak associated with the highest intensity, which is at around 278 cm^{-1}. This peak is related to the O–Ti–O bending vibration.

X-ray photoelectron spectroscopy (XPS) was utilized for the analysis of the atomic composition of the synthesized BBT catalyst. The survey plot of this analysis is shown in Fig. 5a. This figure indicated that the synthesized BBT catalyst is composed of Barium (Ba), Bismuth (Bi), Titanium (Ti), and Oxygen (O) atoms. The carbon (C) indicated in this Fig. 5a is due to environmental contamination. The area under the peaks of individual atoms'

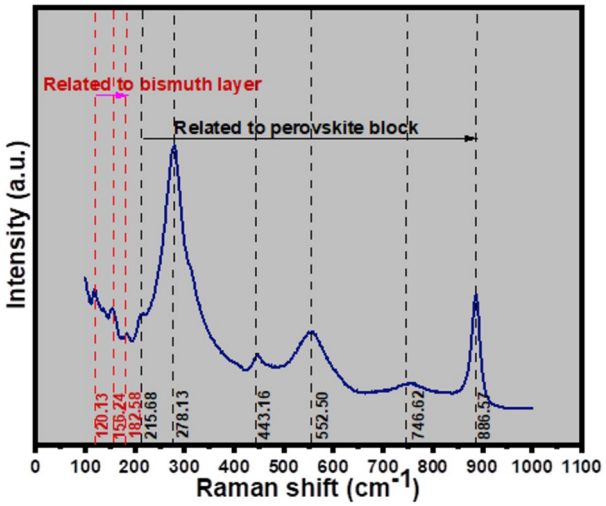

Figure 4. Raman spectrum for BBT.

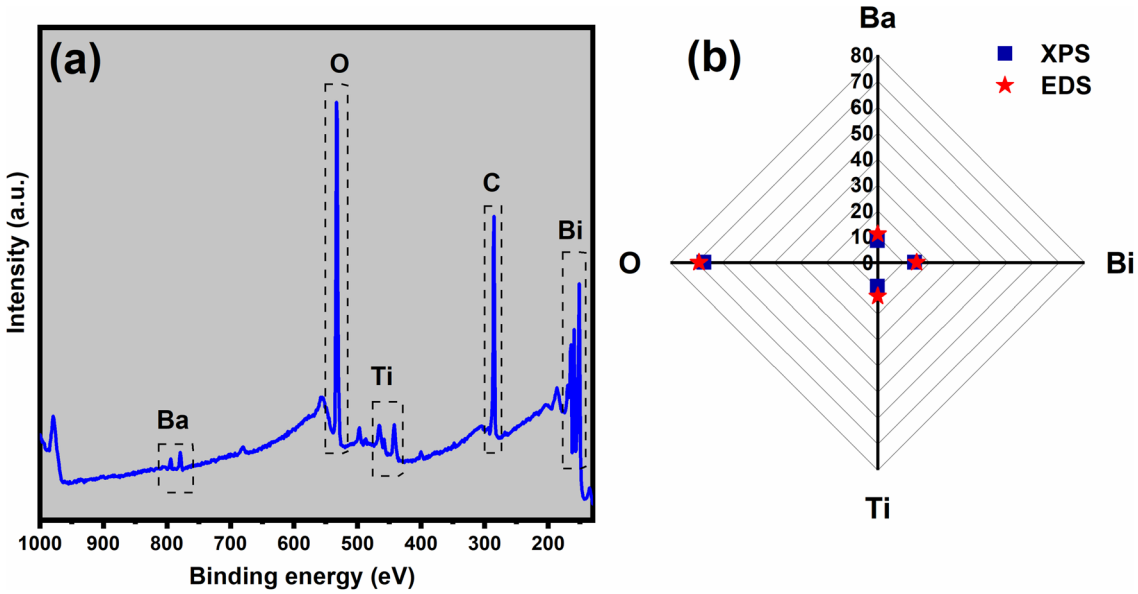

Figure 5. (**a**) X-ray photoelectron spectroscopy (XPS) survey plot, and (**b**) atomic percentage of individual elements (Ba, Bi Ti, O) by EDS and XPS for BBT.

characteristic peaks (Ba, Bi, Ti, and O) represents the total number of atoms. This area is considered for the calculation of the percentage atomic shear of individual atoms. Equation 4 was used for this purpose.

$$Atomic\,\% = \frac{Area\ under\ the\ curve\ of\ atom}{Total\ area\ under\ the\ curve\ of\ all\ atoms}$$

The atomic percentage was calculated and shown in Fig. 5b. It can be seen that the highest atomic percentage is related to the oxygen atom (O), and the lowest atomic percentage is related to the barium (Ba) atom. The atomic percentages of bismuth (Bi) and titanium (Ti) is almost equal and in between the atomic percentage of oxygen and barium. The atomic percentage was also verified by the Energy-dispersive X-ray spectroscopy (EDS) technique. The atomic percentage suggested by EDS is near of atomic percentage suggested by XPS. The hierarchy of the atomic percentages related to the individual atoms fits with the formula of the BBT catalyst. The formula of the BBT consists of 16 atoms (highest) of oxygen so the atomic percentage of oxygen is highest. Furthermore, the atom of barium is the minimum (1) in the formula so the atomic percentage of the barium is minimum. However, the atoms of bismuth and titanium are equal so the atomic percentage of both is almost equal and in between the oxygen and barium.

The XPS spectra of the individual elements are shown in Fig. 6. The carbon was observed in the survey spectra so carbon correction was made in every individual element's XPS spectra. Figure 6a represents the spectrum for the barium element. The peaks of this spectrum were separated and deconvoluted into two individual peaks. These peaks were found at 779 eV and 795 eV and were classified into $Ba3d_{5/2}$ and $Ba3d_{7/2}$ respectively. The separation between these peaks was due to different momentum created by the distinct spins of electrons. Figure 6b represents the spectrum for the bismuth. The peaks of this spectrum were also separated and deconvoluted. The deconvoluted peaks at 159 eV and 165 eV are related to the higher binding state and peaks at 157 eV and 162 eV are related to the lower binding state. The bismuth shows the two binding states because bismuth is present in the perovskite block as well as the bismuth layer. Furthermore, in both cases the surrounding atoms of bismuth are different so bismuth shows two binding states. Figure 6c shows the spectrum of titanium (Ti), the peaks are separated and deconvoluted. The peak at 457.5 eV and 465 eV is related to the $Ti2p_{3/2}$ and $Ti2p_{1/2}$ and the separation between them is due to different electron moments imparted by distinct spins of electrons. The Fig. 6d is related to the oxygen. The peak of this spectrum was deconvoluted and separated into two peaks. The peak near 529 eV is related to the lattice oxygen and the peak near 532 eV is related to the oxygen vacancy. This can be seen from the spectrum that the area under the oxygen vacancy peak is more than the area under the lattice oxygen peak. This indicates that the BBT catalyst contains a significant amount of oxygen vacancy. Previously published studies suggested that there is an increased concentration of oxygen vacancy due to compensating excess bismuth[47]. These increased oxygen vacancies increase the optical properties by narrowing the bandgap.

The catalytic activity of the BBT catalyst was observed through UV-visual spectroscopy. The MB dye solution's characteristic peak was found at 663 nm. The absorbance (height) of the characteristic peaks is an indication of the concentration of the MB dye in the aqueous solution. Figure 7 shows the absorbance vs. wavelength plot for tribocatalysis and piezocatalysis. In this figure, it is indicated that as the time of reaction propagates, the absorbance of the MB dye solution decreases. Which is an indication of a decreasing concentration of MB dye. Figure 7a is related to the tribocatalysis of the MB dye solution and Fig. 7b is related to the piezocatalysis of the MB dye solution. The tribocatalysis experiments were run for 12 h and piezocatalysis experiments were run for 2 h.

Figure 8 indicates the $\ln(C_0/C)$ plot for both catalytic reactions. These plots were generated by using Eq. 2. A straight line was fitted in this plot. The slope of the straight line indicates the rate constant of the catalytic reaction. Both plots consist of degradation reactions without a catalyst (controlled) to compare with catalytic reactions. Figure 8a is related to the tribocatalysis and Fig. 8b is related to the piezocatalysis. The value of the rate constant for tribocatalysis is 0.169 h^{-1}. Furthermore, the rate constant value for the piezocatalysis is 0.003 min^{-1}. For comparison, the value of the rate constant without any catalyst is 0.016 h^{-1} in the case of tribocatalysis and 0.001 min^{-1} in the case of piezocatalysis.

Equation 1 was used to calculate the percentage degradation by tribocatalysis and piezocatalysis. The degradation efficiency for both catalysts is illustrated in Fig. 9a. This figure shows that tribocatalysis degrades 90% of the

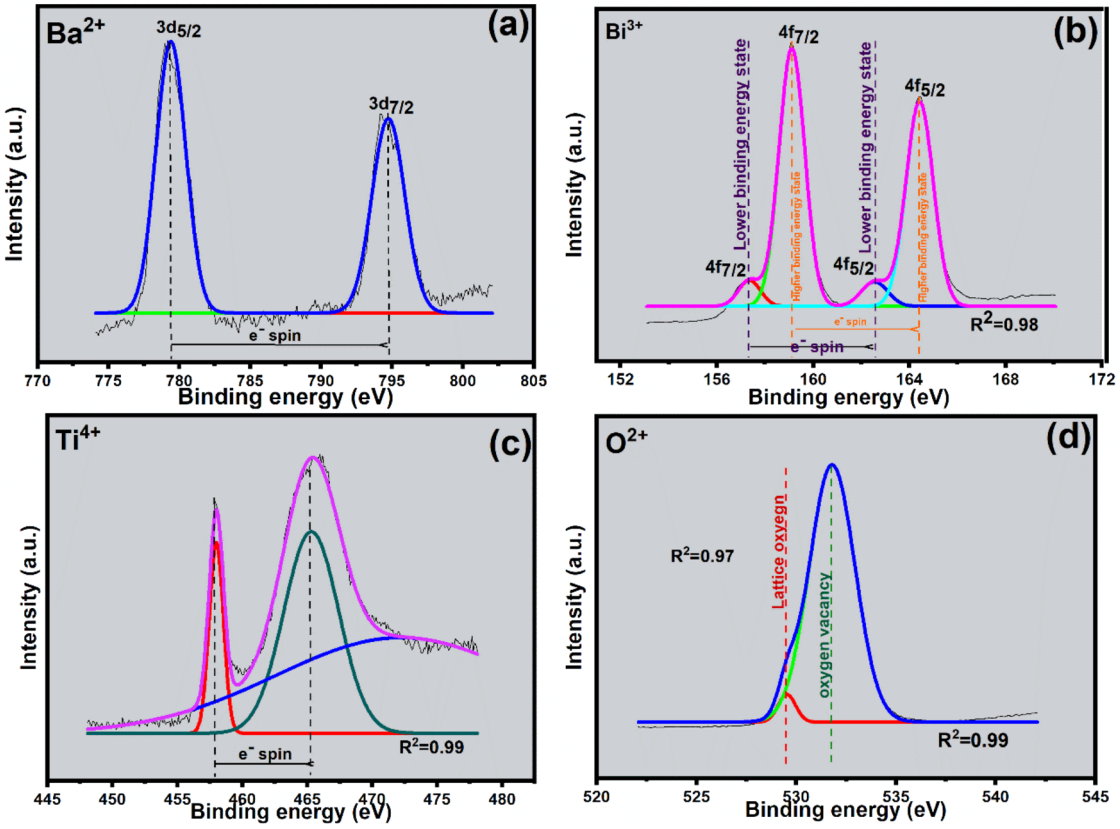

Figure 6. X-ray photoelectron (XPS) plots for individual elements ((**a**) Ba, (**b**) Bi, (**c**) Ti, and (**d**) O) of BBT.

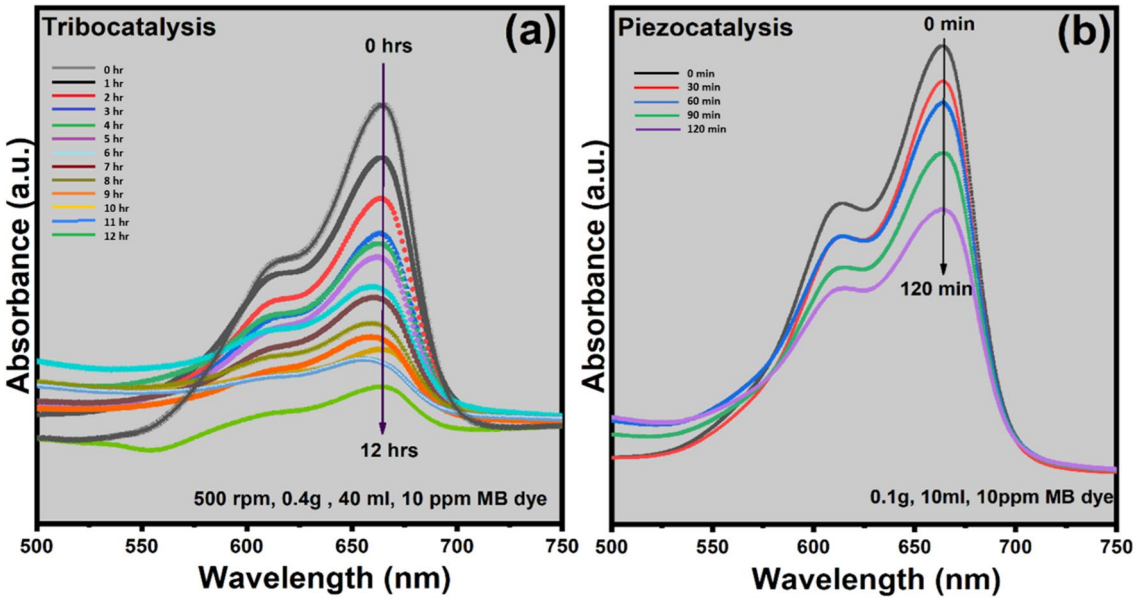

Figure 7. Absorption VS wavelength plots for (**a**) tribocatalysis, and (**b**) piezocatalysis with BBT catalyst.

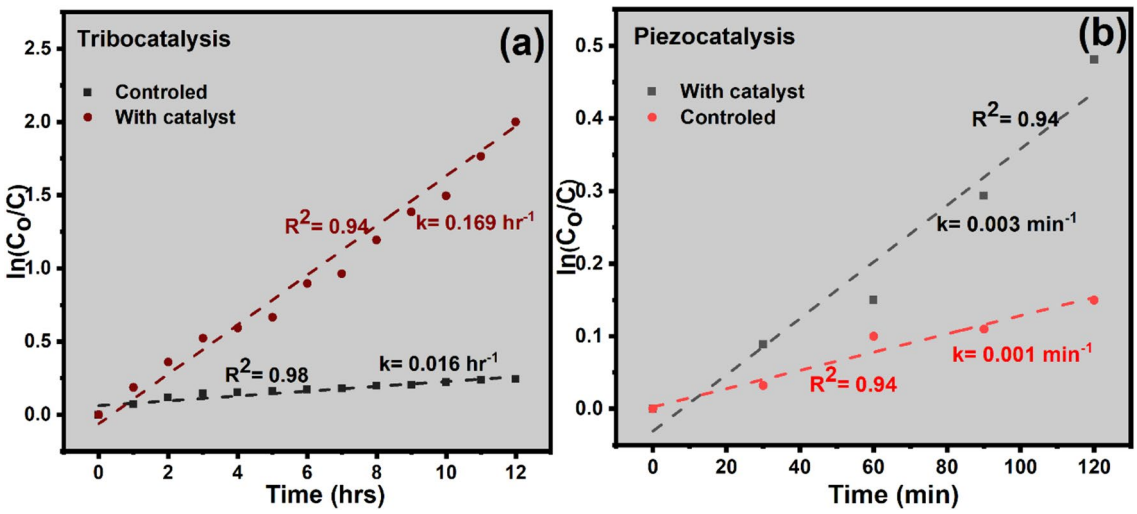

Figure 8. ln (C_o/C) Vs time plot for (**a**) tribocatalysis, and (**b**) piezocatalysis with BBT catalyst.

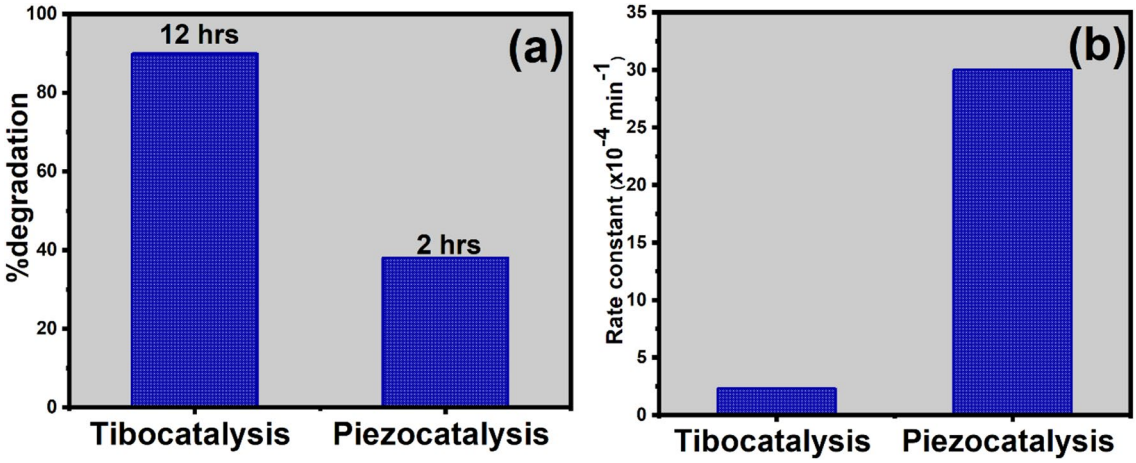

Figure 9. Comparisons of (**a**) percentage degradation, and (**b**) rate constant for tribocatalysis and piezocatalysis.

MB dye in 12 h and piezocatalysis degrades 40% of the MB dye in just 2 h. The discussed degradation efficiencies are not comparable because they were performed for different time periods. So, the rate constant of tribocatalysis and piezocatalysis is shown in Fig. 9b for comparison. This figure indicates that the rate constant for piezocatalysis is 30×10^{-4} min^{-1} whereas the rate constant of the tribocatalytic reaction is 2.3×10^{-4} min^{-1}. The comparison of rate constants of both catalytic reactions suggests that piezocatalysis activity is way more than tribocatalysis activity. This indicates that the piezocatalysis reaction is faster than tribocatalysis. Notably, ultrasonic waves also induce complicated effects that ultimately affect the degradation of dye under sonocatalysis. Similarly, during trobicatalysis experiments, the effect of piezocatalysis can not be ignored. The piezocatalysis and tribocatalysis experiments were performed under different factors such as different volumes of the dye, and different catalyst dosages. Furthermore, the stimuli for the catalyst were also different (piezocatalysis: sonic waves, tribocatalysis: friction). So, it is difficult to state about efficiency as ultrasonication has a significantly large energy source as compared to magnetic stirrer (friction).

The effect of rotation per minute (rpm) on tribocatalytic activity was also evaluated by performing tribocatalysis experiments on different rpm. The results of this analysis are shown in Fig. 10. Figure 10a presents the line fitted in ln (C_o/C) vs time plot. The slope of the line represents the rate constant of the tribocatalytic reaction. This figure indicates that as the rpm of the stirring increases, it leads to an increase in the slope of the fitted line. These results indicate that as stirring speed increases, the tribocatalytic activity also increases. Figure 10b illustrates the percentage degradation of the MB dye aqueous solution. These results indicate that the highest degradation is achieved at the highest stirring speed (700 rpm) and the highest degradation is 94%. Whereas, the lowest degradation is 25% at 300 rpm (lowest). The insight figure of Fig. 10b illustrates the value of the rate constant at different rpm. The highest rate constant is for 700 rpm and the lowest rate constant is for 300 rpm. This study indicates that as the rotational speed of the magnetic stirrer increases, the tribocatalysis activity also increases. The reason behind the increased tribocatalysis is when the stirrer rotates at higher speeds, the shear force and contact pressure at the interface of the catalyst and reactants also increase which promotes the mixing of reactants and enhances the exposure of reactants with active sites on the catalyst. Furthermore, higher rotational speed also generates a high temperature that lowers the activation energy required for the catalysis[63].

The triboelectric series positions materials in an order according to their behavior of getting electrically charged when they are in contact. According to this series, glass is positioned in an extremely positive direction. Whereas, PTFE is positioned in an extremely negative direction. These position of glass and PTFE suggests that when they are in contact, there will be charge transfer due to their different electron affinity. Notably, PTFE is very electronegative. This too much electronegativity attracts the electrons from glass (due to the high electropositivity of glass). When the PTFE disc rubs with glass then electron transfer occurs from the glass to the PTFE disc. In experimental section, it was explained that a PTFE disc glued with a magnetic bead was used to stir the MB dye aqueous solution. In this case, PTFE disc is in friction (rubs) with the glass beaker surface. According to triboelectric series, electron transfer occurs towards PTFE disc. The quantity of electrons increases on PTFE disc surface. This generated charge on PTFE disc reacts with the water molecules present in the MB dye aqueous solution and generates reactive species such as ·OH, O_2^{-}[68]. These reactive species are prerequisites for the degradation of dye molecules. Figure 8a indicates some degradation when none of the catalyst was used. This degradation is due to reactive species generated by the rubbing of PTFE disc surface and glass surface.

When BBT catalyst powder is introduced into the dye solution, it can initiate a chemical reaction due to mechanical frictional energy and enhance the percentage of degradation. When BBT particle traps between a glass beaker and PTFE disc, the positive and negative charged atoms of BBT crystal do not meet with the positive and negative generated charge on the glass and PTFE disc respectively. This unmatching produces the dipole moment and spontaneous polarization occurs in the BBT catalyst. This phenomenon initiates the generation of electron–hole pairs forced in the BBT catalyst due to its small band gap energy. These electron–hole pairs are

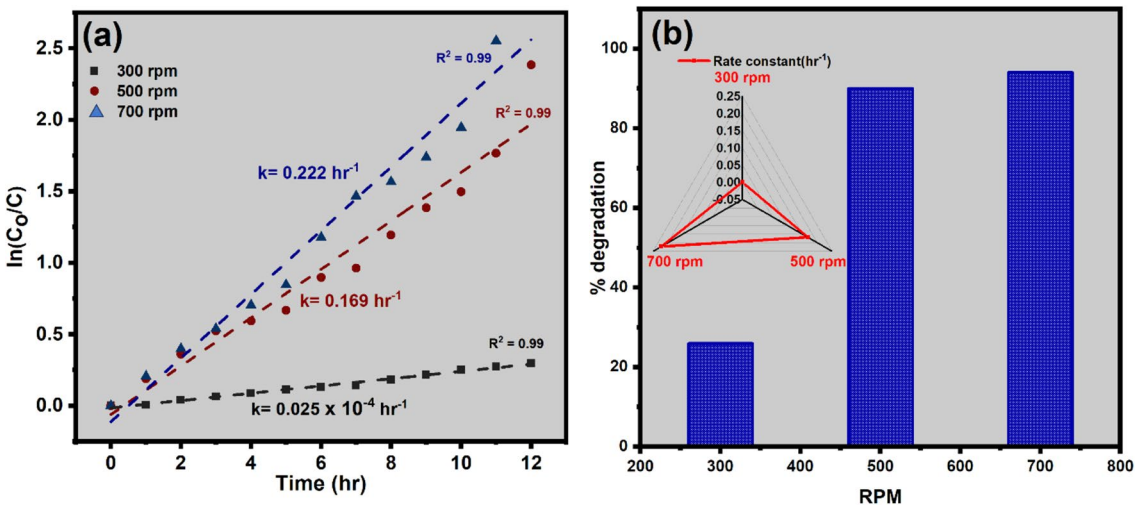

Figure 10. Effect of rpm on tribocatalytic activity (**a**) ln (C_o/C) vs time, and (**b**) comparison of % degradation (insight: rate constant).

forced towards the surface of the catalyst particle. Due to the accumulation of charges on the catalyst surface, a non-zero polarization state occurs in the catalyst particle. When the catalyst reaches the equilibrium, there will not be any electric field throughout the catalyst crystal. The PTFE disc and catalyst particle have different electronegativity, so electron transfer also occurs between PTFE disc and the catalyst particle. This electron transfer generates a non-zero electric field inside the catalyst particle. Notable, catalyst makes electron transfer easier. This electron transfer between the catalyst particle and PTFE disc occurs in the initial period. When the catalyst particle moves, there is a very high possibility of an electron to jumping in the conduction band from the valence band. This process generates the electron–hole pair and initiates the redox reaction for the degradation of MB dye molecule. Another reason behind tribocatalysis is, that friction generates a mechanical force that could overlap the electron cloud and provide easy transfer of electron between atoms. This mechanical force can also excite the catalyst to generate electron–hole pairs. The generation of an electron–hole pair can occur due to two mechanisms, the first is due to bandgap transition and the second is due to electron transfer between atoms. The degradation follows the electron–hole pair generation due to friction (R1). These electrons and holes react with water and generate reactive species (R2 and R3). Generated reactive species react with MB dye molecules and degrade them. In the case of piezocatalysis, the essential electron and hole pairs are generated by the piezoelectric properties of the BBT. The ultrasonicator generates micro shock in the aqueous solution of dye. This microshock exerts a force on the BBT catalyst. Due to the piezoelectric properties of the catalyst, electron and hole pairs were generated which is essential for the dye degradation[46,54,65].

$$\mathrm{BBT} \rightarrow \mathrm{e^-} + \mathrm{h^+} \tag{R1}$$

$$\mathrm{OH^-} + \mathrm{h^+} \rightarrow \cdot \mathrm{OH} \tag{R2}$$

$$\mathrm{O_2} + \mathrm{e^-} \rightarrow \mathrm{O_2^-} \tag{R3}$$

Conclusions

$BaBi_4Ti_4O_{15}$ has demonstrated its catalytic nature triggered using ultrasonic waves and low-frequency stirring motion. Due to its ferroelectric nature, piezocatalysis performance was recorded as 40% degradation in 2 h with a rate constant of about 0.003 min^{-1} under ultrasonication. This is due to the effects of piezocatalysis and sonocatalysis. The catalytic effect was also observed using magnetic stirring at different rpm which can attributed to tribocatalysis. The tribocatalysis degraded 90% of the dye solution in 12 h with a rate constant of about 0.00025 min^{-1}. Tribocatalysis at different rotational speeds suggested that degradation efficiency and rate constant increase with the rotational speed of the magnetic stirrer.

Data availability

The datasets used and/or analysed during the current study available from the corresponding author on reasonable request.

Received: 20 June 2024; Accepted: 25 July 2024
Published online: 06 August 2024

References

1. Ibhadon, A. & Fitzpatrick, P. Heterogeneous photocatalysis: Recent advances and applications. *Catalysts* **3**, 189–218 (2013).
2. Zhu, S. & Wang, D. Photocatalysis: Basic principles, diverse forms of implementations and emerging scientific opportunities. *Adv. Energy Mater.* **7**, 1700841 (2017).
3. Hassaan, M. A. *et al.* Principles of photocatalysts and their different applications: A review. *Top. Curr. Chem.* **381**, 31 (2023).
4. Yang, X. & Wang, D. Photocatalysis: From fundamental principles to materials and applications. *ACS Appl. Energy Mater.* **1**, 6657–6693 (2018).
5. Padmanabhan, N. T. & John, H. Titanium dioxide based self-cleaning smart surfaces: A short review. *J. Environ. Chem. Eng.* **8**, 104211 (2020).
6. Li, X., Wei, H., Song, T., Lu, H. & Wang, X. A review of the photocatalytic degradation of organic pollutants in water by modified TiO2. *Water Sci. Technol.* **88**, 1495–1507 (2023).
7. Haghighi, P. & Haghighat, F. TiO2-based photocatalytic oxidation process for indoor air VOCs removal: A comprehensive review. *Build Environ.* **249**, 111108 (2024).
8. Rafique, M. *et al.* Hydrogen production using TiO_2 -based photocatalysts: A comprehensive review. *ACS Omega* **8**, 25640–25648 (2023).
9. Hernández-Alonso, M. D., Fresno, F., Suárez, S. & Coronado, J. M. Development of alternative photocatalysts to TiO2: Challenges and opportunities. *Energy Environ. Sci.* **2**, 1231 (2009).
10. Porwal, C., Sharma, M., Vaish, R. & Chauhan, V. S. Piezocatalysis dye degradation using SrO-Bi_2O_3 -B_2O_3 glass-ceramics. *ACS Appl. Eng. Mater.* **1**, 295–303 (2023).
11. Gaur, A., Chauhan, V. S. & Vaish, R. Porous BaTiO3 ceramic with enhanced piezocatalytic activity for water cleaning application. *Surf. Interfaces* **36**, 102497 (2023).
12. Singh, G., Sharma, M., Sharma, J. D., Kumar, S. & Vaish, R. Ferroelectric ceramics for pyrocatalytic applications. *Progr. Solid State Chem.* **72**, 100428 (2023).
13. Singh, G., Sharma, M., Bowen, C. & Vaish, R. Ferroelectric ceramics and glass ceramics for photocatalysis. In *Ceramic Science and Engineering* 297–322 (Elsevier, 2022). https://doi.org/10.1016/B978-0-323-89956-7.00019-X.
14. Wang, Y. *et al.* Ferroelectric and photocatalytic properties of Aurivillius phase $Ca_2Bi_4Ti_5O_{18}$. *J. Am. Ceram. Soc.* **104**, 322–328 (2021).
15. Gaur, A., Porwal, C., Boukhris, I., Chauhan, V. S. & Vaish, R. Review on multicatalytic behavior of $Ba_{0.85}Ca_{0.15}Ti_{0.9}Zr_{0.1}O_3$ Ceramic. *Materials* **16**, 5710 (2023).

16. Tang, Q. *et al.* Enhanced piezocatalytic performance of $BaTiO_3$ nanosheets with highly exposed 001 facets. *Adv. Funct. Mater.* https://doi.org/10.1002/adfm.202202180 (2022).
17. Liu, D., Jin, C., Shan, F., He, J. & Wang, F. Synthesizing $BaTiO_3$ nanostructures to explore morphological influence, kinetics, and mechanism of piezocatalytic dye degradation. *ACS Appl. Mater. Interfaces* **12**, 17443–17451 (2020).
18. Masekela, D., Hintsho-Mbita, N. C., Sam, S., Yusuf, T. L. & Mabuba, N. Application of BaTiO3-based catalysts for piezocatalytic, photocatalytic and piezo-photocatalytic degradation of organic pollutants and bacterial disinfection in wastewater: A comprehensive review. *Arab. J. Chem.* **16**, 104473 (2023).
19. Gaur, A., Chauhan, V. S. & Vaish, R. Porous BaTiO3 ceramic with enhanced piezocatalytic activity for water cleaning application. *Surfaces Interfaces* **36**, 102497 (2023).
20. Gaur, A., Porwal, C., Singh, D., Chauhan, V. S. & Vaish, R. Facilitating flexoelectric effect in BaTiO3 ceramic for pollutant removal application via piezocatalysis process. *Colloids Surf. A Physicochem. Eng. Asp.* **689**, 133563 (2024).
21. Porwal, C. *et al.* Piezocatalytic dye degradation using Bi2O3-ZnO-B2O3 glass-nanocomposites. *J. Mater. Res. Technol.* **21**, 2028–2037 (2022).
22. Bai, Y., Zhao, J., Lv, Z. & Lu, K. Enhanced piezocatalytic performance of ZnO nanosheet microspheres by enriching the surface oxygen vacancies. *J. Mater. Sci.* **55**, 14112–14124 (2020).
23. Sharma, A., Bhardwaj, U. & Kushwaha, H. S. ZnO hollow pitchfork: coupled photo-piezocatalytic mechanism for antibiotic and pesticide elimination. *Catal. Sci. Technol.* **12**, 812–822 (2022).
24. Troia, A., Galati, S., Vighetto, V. & Cauda, V. Piezo/sono-catalytic activity of ZnO micro/nanoparticles for ROS generation as function of ultrasound frequencies and dissolved gases. *Ultrason Sonochem* **97**, 106470 (2023).
25. Ning, X. *et al.* Effective promoting piezocatalytic property of zinc oxide for degradation of organic pollutants and insight into piezocatalytic mechanism. *J. Colloid Interface Sci.* **577**, 290–299 (2020).
26. Singh, G., Sharma, M. & Vaish, R. Exploring the piezocatalytic dye degradation capability of lithium niobate. *Adv. Powder Technol.* **31**, 1771–1775 (2020).
27. Singh, G., Sharma, M. & Vaish, R. Flexible Ag@$LiNbO_3$ /PVDF composite film for piezocatalytic dye/pharmaceutical degradation and bacterial disinfection. *ACS Appl. Mater. Interfaces* **13**, 22914–22925 (2021).
28. Zhang, A. *et al.* Ultrasonic vibration driven piezocatalytic activity of lead-free $K_{0.5}Na_{0.5}NbO_3$ materials. *Ceram. Int.* **45**, 22486–22492 (2019).
29. Fan, F.-R., Xie, S., Wang, G.-W. & Tian, Z.-Q. Tribocatalysis: Challenges and perspectives. *Sci. China Chem.* **64**, 1609–1613 (2021).
30. Yu, H. *et al.* Tribocatalytic degradation of organic pollutants using Fe_2O_3 nanoparticles. *ACS Appl. Nano Mater.* **6**, 14364–14373 (2023).
31. Gaur, A., Porwal, C., Chauhan, V. S. & Vaish, R. Synergic effect of photocatalysis and tribocatalysis for dye degradation by $BaTiO_3$ ceramics. *J. Am. Ceram. Soc.* **107**, 2393–2406 (2024).
32. Li, X. *et al.* Tribocatalysis mechanisms: Electron transfer and transition. *J. Mater. Chem. A Mater.* **11**, 4458–4472 (2023).
33. Zhou, Y., Deng, W., Xu, J. & Chen, J. Engineering materials at the nanoscale for triboelectric nanogenerators. *Cell Rep. Phys. Sci.* **1**, 100142 (2020).
34. Sun, E. *et al.* Magnetic material in triboelectric nanogenerators: A review. *Nanomaterials* **14**, 826 (2024).
35. Zhang, R. & Olin, H. Advances in inorganic nanomaterials for triboelectric nanogenerators. *ACS Nanosci. Au* **2**, 12–31 (2022).
36. Munirathinam, P. *et al.* A comprehensive review on triboelectric nanogenerators based on real-time applications in energy harvesting and Self-Powered sensing. *Mater. Sci. Eng. B* **297**, 116762 (2023).
37. Gaur, A., Porwal, C., Chauhan, V. S. & Vaish, R. Synergic effect of photocatalysis and tribocatalysis for dye degradation by $BaTiO_3$ ceramics. *J. Am. Ceram. Soc.* https://doi.org/10.1111/jace.19565 (2023).
38. Chong, J., Tai, B. & Zhang, Y. Tribocatalysis effect based on ZnO with various specific surface areas for dye degradation. *Chem. Phys. Lett.* **835**, 140998 (2024).
39. Wu, M. *et al.* Tribocatalysis of homogeneous material with multi-size granular distribution for degradation of organic pollutants. *J. Colloid Interface Sci.* **622**, 602–611 (2022).
40. Sun, C. *et al.* Tribocatalytic degradation of dyes by tungsten bronze ferroelectric $Ba_{2.5}Sr_{2.5}Nb_8Ta_2O_{30}$ submicron particles. *RSC Adv.* **11**, 13386–13395 (2021).
41. Tang, Q. *et al.* Enhanced tribocatalytic degradation of dye pollutants through governing the charge accumulations on the surface of ferroelectric barium zirconium titanate particles. *Nano Energy* **100**, 107519 (2022).
42. Zhu, Z. *et al.* Ferroelectric field enhanced tribocatalytic hydrogen production and RhB dye degradation by tungsten bronze ferroelectrics. *Nanoscale* https://doi.org/10.1039/D4NR00868E (2024).
43. Bobić, J. D. *et al.* Lead-free BaBi4Ti4O15 ceramics: Effect of synthesis methods on phase formation and electrical properties. *Ceram. Int.* **41**, 309–316 (2015).
44. Zhang, W. *et al.* Ferroelectric mesocrystalline $BaTiO_3$ /$BaBi_4Ti_4O_{15}$ nanocomposite: formation mechanism, nanostructure, and anomalous ferroelectric response. *Nanoscale* **11**, 3837–3846 (2019).
45. Khokhar, A., Goyal, P. K., Thakur, O. P. & Sreenivas, K. Effect of excess of bismuth doping on dielectric and ferroelectric properties of BaBi4Ti4O15 ceramics. *Ceram. Int.* **41**, 4189–4198 (2015).
46. Kumar, P. & Vaish, R. Effect of poling on piezocatalytic activity of SrBi4Ti4O15 in dye degradation. *Mater. Today Commun.* **39**, 108803 (2024).
47. Kumar, P. & Vaish, R. Enhanced photocatalytic activity in BaBi4Ti4O15 with excess Bi2O3. *Surf. Interfaces* **40**, 103082 (2023).
48. Chakrabarti, A., Bera, J. & Sinha, T. P. Dielectric properties of BaBi4Ti4O15 ceramics produced by cost-effective chemical method. *Phys. B Condens. Matter.* **404**, 1498–1502 (2009).
49. Lee, J.-K., Park, B. & Hong, K.-S. Effect of excess Bi2O3 on the ferroelectric properties of SrBi2Ta2O9 ceramics. *J. Appl. Phys.* **88**, 2825–2829 (2000).
50. Chen, T.-C., Li, T., Zhang, X. & Desu, S. B. The effect of excess bismuth on the ferroelectric properties of $SrBi_2Ta_2O_9$ thin films. *J. Mater. Res.* **12**, 1569–1575 (1997).
51. Simões, A. Z., da Costa, G. C. C., Ramírez, M. A., Varela, J. A. & Longo, E. Effect of the excess of bismuth on the morphology and properties of the BaBi2Ta2O9 ceramics. *Mater. Lett.* **59**, 656–661 (2005).
52. Khokhar, A., Mahesh, M. L. V., James, A. R., Goyal, P. K. & Sreenivas, K. Sintering characteristics and electrical properties of BaBi4Ti4O15 ferroelectric ceramics. *J. Alloys Compd.* **581**, 150–159 (2013).
53. Rout, S. K. *et al.* Phase transition in ABi4Ti4O15 (A=Ca, Sr, Ba) Aurivillius oxides prepared through a soft chemical route. *J. Appl. Phys.* **105**, 024105 (2009).
54. Kumar, P. *et al.* Effect of poling on photocatalysis, piezocatalysis, and photo-piezo catalysis performance of BaBi 4 Ti 4 O 15 ceramics. *Global Challenges* https://doi.org/10.1002/gch2.202200142 (2023).
55. Kumar, S., Kundu, S., Ochoa, D. A., Garcia, J. E. & Varma, K. B. R. Raman scattering, microstructural and dielectric studies on Ba1−xCaxBi4Ti4O15 ceramics. *Mater. Chem. Phys.* **136**, 680–687 (2012).
56. Kroumova, E. *et al.* Bilbao crystallographic server : Useful databases and tools for phase-transition studies. *Phase Trans.* **76**, 155–170 (2003).
57. Dobal, P. S. & Katiyar, R. S. Studies on ferroelectric perovskites and Bi-layered compounds using micro-Raman spectroscopy. *J. Raman Spectrosc.* **33**, 405–423 (2002).

58. Hao, H., Liu, H. & Ouyang, S. Structure and ferroelectric property of Nb-doped SrBi4Ti4O15 ceramics. *J. Electroceram.* **22**, 357–362 (2009).
59. Hao, H., Liu, H. X., Cao, M. H., Min, X. M. & Ouyang, S. X. Study of A-site doping of SrBi4Ti4O15 Bi-layered compounds using micro-Raman spectroscopy. *Appl. Phys. A* **85**, 69–73 (2006).
60. Huang, S., Li, Y., Feng, C., Gu, M. & Liu, X. Dielectric and structural properties of layer-structured Sr 1–x Ca x Bi 2 Nb 2 O 9. *J. Am. Ceram. Soc.* **91**, 2933–2937 (2008).
61. Liu, G. Z., Wang, C., Gu, H. S. & Lu, H. B. Raman scattering study of La-doped SrBi2 Nb2 O9 ceramics. *J. Phys. D Appl. Phys.* **40**, 7817–7820 (2007).
62. Graves, P. R., Hua, G., Myhra, S. & Thompson, J. G. the raman modes of the aurivillius phases: Temperature and polarization dependence. *J Solid State Chem* **114**, 112–122 (1995).
63. Gaur, A., Porwal, C., Chauhan, V. S. & Vaish, R. Tribocatalytic investigation of BaTiO3 for dye removal from water. *J. Mater. Sci. Mater. Electron.* **34**, 2154 (2023).
64. Baytekin, B., Baytekin, H. T. & Grzybowski, B. A. What really drives chemical reactions on contact charged surfaces?. *J. Am. Chem. Soc.* **134**, 7223–7226 (2012).
65. Kumar, P. & Vaish, R. Effect of poling and excess Bi2O3 on piezocatalysis by BaBi4Ti4O15. *J. Mater. Sci. Mater. Electron.* **34**, 2278 (2023).

Acknowledgements

The authors extend their appreciation to the Deanship of Research and Graduate Studies at King Khalid University for funding this work through Large Groups Project under grant number RGP.2/36/45. Also, this research was funded by Princess Nourah bint Abdulrahman University Researchers Supporting Project number (PNURSP2024R19), Princess Nourah bint Abdulrahman University, Riyadh, Saudi Arabia. This work was also supported by the Korea Institute of Energy Technology Evaluation and Planning (KETEP) and the Ministry of Trade, Industry & Energy (MOTIE) of the Republic of Korea (No. 20224000000440, Sector Coupling Energy Industry Advancement Manpower Training Program).

Author contributions

P.K., N.S.A., A.G., Karan, R.V., A.A., H.O., Y.H.J., T.H.S., A.K., W.C.L., P.K., A.G., Karan performed experiments and drafted manuscript, N.S.A., R.V., A.A., H.O. designed the experiments, Y.H.J., T.H.S., A.K., W.C.L. overall supervised.

Competing interests

The authors declare no competing interests.

Additional information

Correspondence and requests for materials should be addressed to R.V. or A.K.

Reprints and permissions information is available at www.nature.com/reprints.

Publisher's note Springer Nature remains neutral with regard to jurisdictional claims in published maps and institutional affiliations.